Quench Dynamics and Hall Response of Interacting Chern Insulators
Supplemental Material

Michael Schüler,[1] Jan Carl Budich,[2] and Philipp Werner[1]

[1]*Department of Physics, University of Fribourg, 1700 Fribourg, Switzerland*
[2]*Institute of Theoretical Physics, Technische Universität Dresden, 01062 Dresden, Germany*

I. THEORETICAL METHODS

A. Time-dependent nonequilibrium Green's function approach

The time-dependent nonequilibrium Green's function (TD-NEGF) method is based on solving the Kadanoff-Baym equations (KBEs) for the single-particle Green's function (SPGF):

$$\left(\mathrm{i}\partial_t - \mathbf{h}(\mathbf{k};t)\right)\mathbf{G}(\mathbf{k};t,t') = \delta_{\mathcal{C}}(t,t') + \int_{\mathcal{C}} \mathrm{d}\bar{t}\,\mathbf{\Sigma}(\mathbf{k};t,\bar{t})\mathbf{G}(\mathbf{k};\bar{t},t')\,. \tag{1}$$

The time arguments of the SPGF $\mathbf{G}(\mathbf{k};t,t')$ lie on the L-shaped Kadanoff-Baym contour $\mathcal{C}$. In practice, we solve this equation by introducing a set of two-time correlators [1]. The resulting KBEs are

$$\mathrm{i}\partial_t \mathbf{G}^{>}(\mathbf{k};t,t') = \mathbf{h}(\mathbf{k};t)\mathbf{G}^{>}(\mathbf{k};t,t') + [\mathbf{\Sigma}(\mathbf{k}) * \mathbf{G}(\mathbf{k})]^{>}(t,t')\,, \tag{2a}$$

$$-\mathrm{i}\partial_t \mathbf{G}^{<}(\mathbf{k};t',t) = \mathbf{G}^{>}(\mathbf{k};t',t)\mathbf{h}(\mathbf{k};t) + [\mathbf{G}(\mathbf{k}) * \mathbf{\Sigma}(\mathbf{k})]^{<}(t',t)\,, \tag{2b}$$

$$\mathrm{i}\partial_t \mathbf{G}^{\rceil}(\mathbf{k};t,\tau) = \mathbf{h}(\mathbf{k};t)\mathbf{G}^{\rceil}(\mathbf{k};t,\tau) + [\mathbf{\Sigma}(\mathbf{k}) * \mathbf{G}(\mathbf{k})]^{\rceil}(t,\tau)\,. \tag{2c}$$

Here, the standard Langreth rules [1] define the convolution

$$\begin{aligned}[\mathbf{A}(\mathbf{k}) * \mathbf{B}(\mathbf{k})]^{\gtrless}(t,t') = &\int_0^t \mathrm{d}\bar{t}\,\mathbf{A}^{\mathrm{R}}(\mathbf{k};t,\bar{t})\mathbf{B}^{\gtrless}(\mathbf{k};\bar{t},t') \\ &+ \int_0^{t'} \mathrm{d}\bar{t}\,\mathbf{A}^{\gtrless}(\mathbf{k};t,\bar{t})\mathbf{B}^{\mathrm{A}}(\mathbf{k};\bar{t},t') \\ &- \mathrm{i}\int_0^{\beta} \mathrm{d}\tau\,\mathbf{A}^{\rceil}(\mathbf{k};t,\tau)\mathbf{B}^{\lceil}(\mathbf{k};\tau,t')\end{aligned}$$

and

$$\begin{aligned}[\mathbf{A}(\mathbf{k}) * \mathbf{B}(\mathbf{k})]^{\rceil}(t,\tau) = &\int_0^t \mathrm{d}\bar{t}\,\mathbf{A}^{\mathrm{R}}(\mathbf{k};t,\bar{t})\mathbf{B}^{\rceil}(\mathbf{k};\bar{t},\tau) \\ &+ \int_0^{\beta} \mathrm{d}\tau'\,\mathbf{A}^{\rceil}(\mathbf{k};t,\tau')\mathbf{B}^{\mathrm{M}}(\mathbf{k};\tau'-\tau)\,.\end{aligned}$$

For a given choice of the many-body self-energy $\mathbf{\Sigma}(\mathbf{k})$, one first obtains the Matsubara SPGF $\mathbf{G}^{\mathrm{M}}(\mathbf{k};\tau)$ which captures initial correlations. With the initial conditions thus determined, the KBEs (2) govern the real-time evolution.

For the quench setup employed the in the main text, the KBEs (2) simplify due to the lack of initial correlations, leading to $\mathbf{\Sigma}^{\rceil}(\mathbf{k};t,\tau) = 0$. In this scenario, the initial conditions (keeping track of orbital and spin indices) are determined by

$$\begin{aligned}G^{<}_{\alpha\alpha'\sigma}(\mathbf{k};0,0) &= \mathrm{i}\widetilde{\rho}_{\alpha\alpha'\sigma}(\mathbf{k})\,, \\ G^{>}_{\alpha\alpha'\sigma}(\mathbf{k};0,0) &= -\mathrm{i}(\delta_{\alpha\alpha'} - \widetilde{\rho}_{\alpha\alpha'\sigma}(\mathbf{k}))\,,\end{aligned} \tag{3}$$

where $\widetilde{\rho}_{\alpha\alpha'\sigma}(\mathbf{k})$ is the density matrix corresponding to the (uncorrelated) pre-quench equilibrium state.

In either setup, the KBEs (2) are solved with an in-house massively-parallel computer code (used also in Ref. [2]) based on a fifth-order predictor-corrector scheme. An equidistant time step of $\Delta t = 0.05$ was used, ensuring the convergence of all observables.

B. Generalized Kadanoff-Baym ansatz

The generalized Kadanoff-Baym ansatz (GKBA) [3] reduces the KBEs (2) to an equation of motion for the density matrix

$$\frac{\mathrm{d}}{\mathrm{d}t}\boldsymbol{\rho}(\mathbf{k};t) = -\mathrm{i}\left[\mathbf{h}^{\mathrm{MF}}(t), \boldsymbol{\rho}(\mathbf{k};t)\right] - \mathbf{I}(\mathbf{k},t)\,, \tag{4}$$

where the collision term $\mathbf{I}(\mathbf{k},t)$ is defined by

$$\mathbf{I}(\mathbf{k},t) = [\mathbf{\Sigma}(\mathbf{k}) * \mathbf{G}(\mathbf{k})]^{<}(t,t) + \mathrm{h.\,c.}\,. \tag{5}$$

The time off-diagonal SPGF required for computing the collision integral (5) are reconstructed by the GKBA

$$\begin{aligned}-\mathrm{i}\mathbf{G}^{\gtrless}(\mathbf{k};t,t') = &\mathbf{G}^{\mathrm{R}}(\mathbf{k};t,t')\mathbf{G}^{\gtrless}(\mathbf{k};t,t') \\ &- \mathbf{G}^{\gtrless}(\mathbf{k};t,t')\mathbf{G}^{\mathrm{A}}(\mathbf{k};t,t')\,.\end{aligned} \tag{6}$$

We employ the Hatree-Fock (HF) approximation to the retarded SPGF:

$$\begin{aligned}\mathbf{G}^{\mathrm{R}}(\mathbf{k};t,t') &= -\mathrm{i}\theta(t-t')\mathcal{T}\exp\left(\int_{t'}^{t}\mathrm{d}\bar{t}\,\mathbf{h}^{\mathrm{HF}}(\mathbf{k};\bar{t})\right) \\ &\equiv -\mathrm{i}\theta(t-t')\mathbf{U}(\mathbf{k};t,t'),\end{aligned} \tag{7}$$

where $\mathbf{h}^{\mathrm{HF}}(\mathbf{k};\bar{t})$ denotes the mean-field HF Hamiltonian, while $\mathcal{T}$ stands for the time-ordering symbol. The time-evolution operator $\mathbf{U}(\mathbf{k};t,t')$ defined by Eq. (7) is computed using the semigroup property $\mathbf{U}(\mathbf{k};t_n+\Delta t,t_j) = \mathbf{U}(\mathbf{k};t_n+\Delta t,t_n)\mathbf{U}(\mathbf{k};t_n,t_j)$ on a uniform mesh of time points $t_n = n\Delta t$. The propagator $\mathbf{U}(\mathbf{k};t_n+\Delta t,t_n)$ is computed using the fourth-order commutator-free matrix-exponential method [4]. The GKBA equation (6) is solved using an in-house highly accurate computer code. A fixed time step $\Delta t = 0.05$ was used in all calculations.

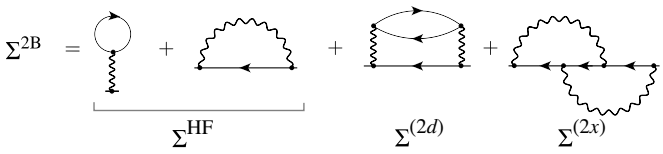

FIG. 1. Feynmann diagrams representing the second-Born approximation, consisting of the Hatree-Fock (first two diagrams), direct (third diagram) and exchange (last diagram) contribution.

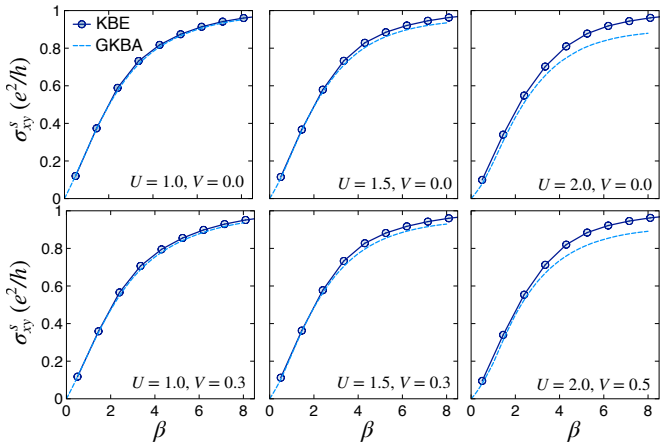

FIG. 2. Hall conductance of the spinfull $\mathbb{Z}_2$ insulator in thermal equilibrium as a function of the inverse temperature β for different values of the local interaction parameters U and V. For the KBE calculations the system size is $N_k = 32\times32$, while we used $N_k = 128\times128$ for the GKBA. In both cases the convergence towards the thermodynamic limit has been checked.

C. Self-energy: second-Born approximation

All results in the main text have been obtained within the second-Born approximation (2BA). The corresponding diagrammatic representation is shown in Fig. 1.

Using the standard Feynmann rules [1], the diagrams for the 2BA have been cast into mathematical expressions on the Kadanoff-Baym contour and implemented in our computer codes. A general explicit expression in the Wannier representation can be found, for instance, in Ref. [5].

For nonlocal interactions, however, the large computational effort to treat the exchange diagram prevents us from employing the full 2BA in this case. Therefore, we have omitted $\Sigma^{(2x)}$ in the treatment of the Chern insulators with nonlocal interactions. For all other cases, we have confirmed that not including the exchange diagrams leads to very small quantitative changes. Hence, all statements in the main text on thermalization still remain valid. Note that even without including the exchange diagram, the resulting 2BA is still energy conserving.

II. CALCULATION OF THE EQUILIBRIUM HALL CONDUCTANCE

In order to investigate if the steady-state Hall conductance discussed in the main text corresponds to thermal equilibrium, we computed the equilibrium Hall conductance as a function of temperature. Following Ref. [6], we have prepared the initial density matrix $\rho_\sigma(\mathbf{k}, t = 0)$ with respect to the topologically nontrival post-quench Hamiltonian including interactions on the mean-field level. Propagating using the GKBA while adiabatically switching on the 2BA self-energy yields a correlated initial state $\rho_\sigma(\mathbf{k}, t_{\rm switch})$. Applying the probe electric field $E_y(t) = F_0(1 - e^{-(t-t_{\rm switch})/\tau_0})$ ($E_y(t) = 0$ for $t < t_{\rm switch}$) after the interactions are switched on then yields the equilibrium Hall conductance via $\sigma_{xy} = \lim_{t\to\infty} J_x(t)/F_0$. This procedure is performed for a set of inverse temperatures β. Repeating the adiabatic switching procedure without probe field leads to a constant total energy $E_{\rm tot}$, which yields the temperature dependence of $E_{\rm tot}$. The function $E_{\rm tot}(\beta)$ is then used to determine the effective temperature $T_{\rm eff}$. The adiabatic switching was realized using the double-exponential switch-on function from Ref. [5], using a time interval of $t_{\rm switch} = 40$.

Within the full KBE treatment, on the other hand, the preparation of a correlated initial state in thermal equilibrium is accomplished by solving the Dyson equation for the Matsubara SPGF $\mathbf{G}^{\rm M}(\mathbf{k};\tau)$. The total energy $E_{\rm tot}(\beta)$ is computed via the Galitskii-Migdal formula [1]. The time evolution in the presence of the probe field $E_y(t) = F_0(1-e^{-(t/\tau_0})$ is then obtained by solving the full set of the KBEs (2).

Figure 2 shows the spin Hall conductance of the $\mathbb{Z}_2$ insulator in thermal equilibrium, comparing the full KBE and the GKBA treatment. The agreement is very good for smaller β (higher temperature, that is) and weaker interactions, while deviations become apparent for low temperature and stronger interaction. In particular, the full KBE treatment recovers the limit $\sigma^s_{xy} \to e^2/h$ for $\beta \to \infty$. This is consistent with the fact that the topological properties cannot be altered by (weak) electron-electron interactions. In contrast, the GKBA does not reproduce this limit correctly. Nevertheless, since the effective temperatures in the quench setup studied in the main text are quite high (typically $\beta \sim 1$ to $\beta \sim 2$), the GKBA provides an accurate description.

III. DEPENDENCE ON PRE- AND POST-QUENCH STATE

In this section we map out the unique features of the nonequilibrium phase transition from the trivial band insulator (BI) to the topological insulator (TI). We will show that this transition is determined by (i) the build-up of a significant Hall response which approaches the quantized value in the limit of a slow quench, and (ii) the purity gap closing marking the topological transition of the single-particle density matrix, indicated by the pseudospin $r_z(\mathbf{k};t)$ crossing zero at the Γ point. To illustrate how the aforementioned properties are capable of distinguishing different quench setups, we have performed additional simulations for all possible combinations of pre- and post-quench phases. The parameters are analogous to those

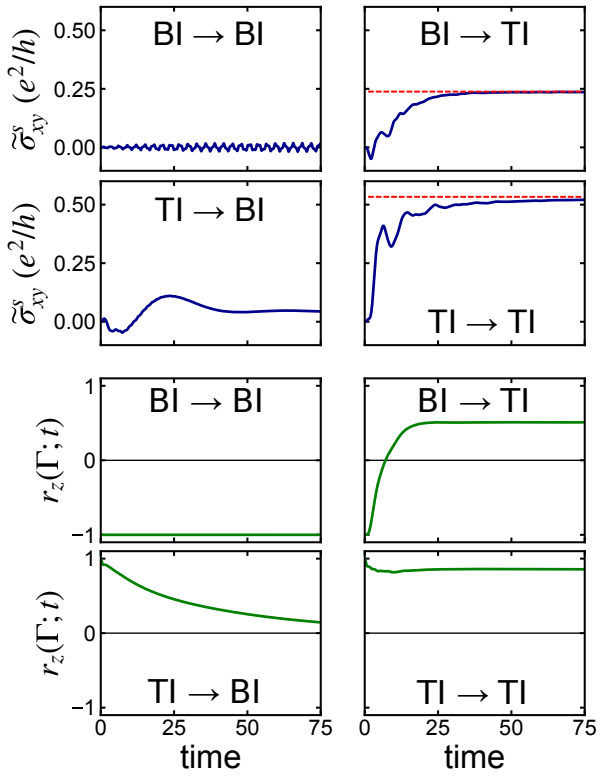

FIG. 3. Upper panels: Nonequilibrium Hall response for quenches from BI to BI (upper left), BI to TI (upper right) , TI to BI (lower left), and TI to TI (lower right). The red-dashed lines correspond to thermal equilibrium Hall conductance. Lower panels: pseudospin component r_z at the Γ point for the same set-up. Calculations have been performed using the GKBA on a $N_k = 220 \times 220$ cluster.

in the main text: we consider the spinfull $\mathbb{Z}_2$ insulator with $U = 1.5$ and $V = 0$. The results are shown in Fig. 3.

In particular, considering the quench from a BI with mass parameter $M_{\rm pre} = -4.0$ to a BI with $M_{\rm post} = -3.5$, we observe a dominantly oscillatory (spin) Hall response $\widetilde{\sigma}^s_{xy}(t)$ induced by an electric probe field implemented as described in the main text. As $t \to \infty$ ($\widetilde{\sigma}^s_{xy}(t \to \infty)$ corresponds to the static Hall effect), the Hall response vanishes. However, note that the BI thermalizes very slowly due to the large band gap, which suppresses inter-band relaxation. Therefore, the complete thermalization is beyond the accessible time window. Nevertheless, Fig. 3 shows that no constant steady-state Hall conductance is reached. Similarly, the pseudospin $r_z(\Gamma;t)$ does not undergo a sign change – hence, the gap of the single-particle density matrix does not close and no topological phase transition occurs. After complete thermalization, the system relaxes to the BI governed by $M_{\rm post}$ (and the mean-field contributions) with an effective temperature $T_{\rm eff}$.

This is in contrast to the quench BI → TI, where the purity gap closes (indicated by $r_z(\Gamma;t)$ changing sign from negative to positive) and a constant Hall response is established in the equilibrated state.

It is also interesting to analyze the transition TI → BI. In this case, $r_z(\Gamma;t)$ changes sign from positive to negative, indicating the topological phase transition from topological to trivial on the level of the density matrix. In accordance with this behavior, the steady-state Hall response approaches zero. Again, we remark that the thermalization in the BI is very slow due to the large band gap, which suppresses inter-band scattering. Therefore, the full thermalization of the Hall response and the purity gap closing occur on a time scale which is longer than what is computationally accessible.

For the transition TI ($M_{\rm pre} = -1.5$) → TI ($M_{\rm pre} = -1.0$), Fig. 3 shows – as expected – the build-up of a Hall response approaching the thermal equilibrium value. Because the system is excited, the steady state yields a Hall conductance smaller than one. The pseudospin marker $r_z(\Gamma;t)$ stays positive for all times.

IV. EFFECTIVE TEMPERATURE

The effective temperature used to compute equilibrium properties in the main text is governed by two factors:

1. The energy injected into the system by the quench. It is defined as $\Delta E = E_{\rm quench} - E_0$, where E_0 is the energy of the post-quench Hamiltonian at zero temperature, while $E_{\rm quench}$ is the energy right after the quench.

2. The dependence of the total energy $E_{\rm post}(\beta)$ of the post-quench system in thermal equilibrium on the inverse temperature β. The effective (inverse) temperature $\beta_{\rm eff}$ is determined by $E_{\rm quench} = E_{\rm post}(\beta_{\rm eff})$.

A. Sudden quench

In the scenario of a sudden quench of the gap parameter $M_{\rm pre} \to M_{\rm post}$, as studied in the main text, the effective temperature is predominantly determined by the post-quench mass parameter $M_{\rm post}$. To illustrate this behavior, we have computed the injected energy and the effective inverse temperature for the spin Chern insulator for $U = 1.5$ and $V = 0$. The findings are, however, generic.

The first row in Fig. 4 shows the dependence of the injected energy ΔE on $M_{\rm pre}$ ($M_{\rm post}$) for fixed $M_{\rm post}$ ($M_{\rm pre}$), see left (right) panel. As can be infered from Fig. 4, ΔE varies only very little with $M_{\rm pre}$. This can be understood by the fact that the Bloch wave-functions for the BI are almost completely composed of pure E or H bands. Hence, the initial occupation after the quench – which is determined by the pre-quench density matrix – depends only weakly on $M_{\rm pre}$. In contrast, the post-quench gap parameter $M_{\rm post}$ plays a decisive role: the smaller $M_{\rm post}$, the less energy is injected. Comparing $E_{\rm quench}$ to the temperature dependent $E_{\rm post}(\beta)$ allows to determine the effective inverse temperature $\beta_{\rm eff}$ (middle panels in Fig. 4).

The electron distribution $f^{\rm eq}_+(\mathbf{k})$ shown in Fig. 1 and Fig. 3 in the main text is computed at the thus determined $\beta_{\rm eff}$ and compared to the time-dependent occupation $f_+(\mathbf{k};t)$. The time evolution of $f_+(\mathbf{k};t)$ approaches the thermal distribution for all cases, except for the case of the Chern insulator with local interactions only.

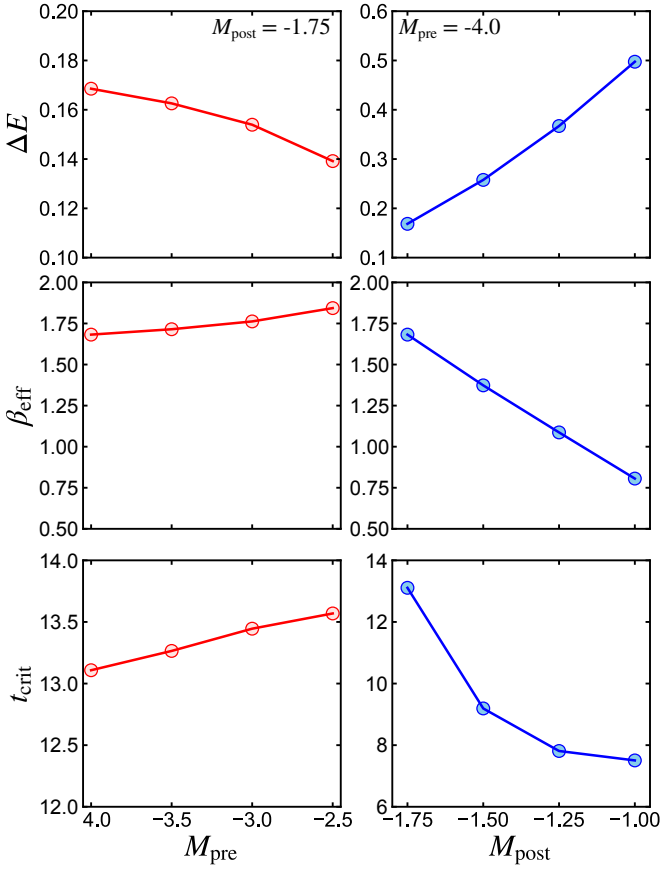

FIG. 4. Quench-injected energy ΔE, effective inverse temperature after thermalization, and critical time for gap closure $t_{\rm crit}$ as a function of the pre-quench mass parameter $M_{\rm pre}$ at fixed $M_{\rm post}$ (plots on the left-hand side), and as a function of $M_{\rm post}$ for fixed $M_{\rm pre}$ (right-hand side). Calculations have been performed using the GKBA on a $N_k = 220 \times 220$ cluster.

In accordance with the behavior of ΔE, the effective inverse temperature is almost independent of the pre-quench state, while a $M_{\rm post}$ closer to the phase boundary $M_{\rm crit} = -2$ leads to a larger $\beta_{\rm eff}$ and thus lower $T_{\rm eff} = 1/\beta_{\rm eff}$. This picture is also consistent with Fig. 4 in the supplemental material, where we have investigated the Hall response for the same parameters. Similarly, we find that the steady-state Hall response is the largest for $M_{\rm post}$ as close to $M_{\rm crit}$ as possible. The pre-quench configuration, on the other hand, has only a very small influence.

One can also work out the dependence of ΔE on the interactions. Right after the quench (at $t = 0$), the total energy is given by

$$E_{\rm quench} = \frac{1}{N_k}\sum_{\mathbf{k}} {\rm Tr}\left[\boldsymbol{\rho}(\mathbf{k};t=0)\mathbf{h}(\mathbf{k})\right] + \frac{1}{2N_k}\sum_{\mathbf{k}} {\rm Tr}\left[\boldsymbol{\rho}(\mathbf{k};t=0)\mathbf{v}^{\rm MF}(\mathbf{k})\right] ,$$

where $\mathbf{v}^{\rm MF}(\mathbf{k})$ is the mean-field term, which depends on the density matrix itself. At $t = 0$, $\boldsymbol{\rho}(\mathbf{k};t=0)$ describes a trivial

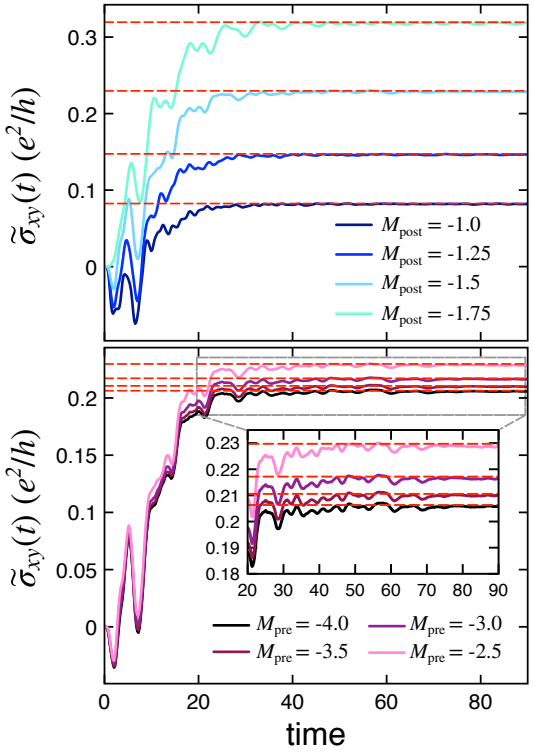

FIG. 5. Nonequilibrium (spin) Hall conductance of the spinfull $\mathbb{Z}_2$ insulator for the same setup as in the main text. In the upper panel, $M_{\rm pre} = -3.5$, while $M_{\rm post} = -1.5$ for the lower panel. The red-dashed lines indicate the corresponding thermal equilibrium. Calculations have been performed using the GKBA on a $N_k = 220 \times 220$ cluster.

state and can thus be approximated as

$$\boldsymbol{\rho}(\mathbf{k};t=0) \approx \begin{pmatrix} 1 & 0 \\ 0 & 0 \end{pmatrix} ,$$

i. e. the E band is fully occupied ($n_E \approx 1$), while the H band is empty ($n_H \approx 0$). Explict checks support this picture. Inserting the explicit form the of mean-field Hamiltonian (taken from the supplemental material), one obtains

$$E_{\rm quench} \approx M_{\rm post} + \frac{U}{2} . \tag{8}$$

In conclusion, the onsite-repulsion U increases $M^{\rm eff}_{\rm post}$, effectively shifting $M_{\rm post}$ to the right in Fig. 4, thus giving rise to lower $\beta_{\rm eff}$ and larger $T_{\rm eff}$.

The steady-state Hall response – determined by $T_{\rm eff}$ – follows the same trend, as demonstrated by Fig. 5. This indicates that the gap size of the pre-quench band insulator plays only a minor role, while the dependence on the post-quench gap parameter $M_{\rm post}$ is much more pronounced. One finds an increasing Hall conductance with $M_{\rm post}$ approaching the phase boundary $M_{\rm post} = -2$. Furthermore, Fig. 5 demonstrates that the system builds up a steady-state Hall response corresponding to thermal equilibrium for any quench from the trivial to the topological regime.

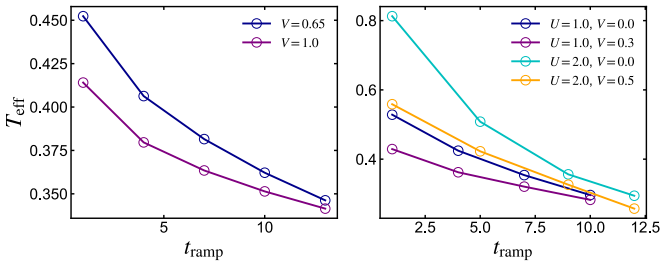

FIG. 6. Effective temperature $T_{\rm eff}$ after thermalization for the Chern insulator with nonlocal interactions (left-hand side) and the $\mathbb{Z}_2$ insulator (right-hand side). The color scheme is consistent with Fig. 4 in the main text. For the Chern insulator and the $\mathbb{Z}_2$ insulator with $U = 1.0$, we used the GKBA on a $N_k = 128 \times 128$ cluster, while the larger interaction $U = 2.0$ has been treated using the full KBEs on a $N_k = 32 \times 32$ cluster.

The second, albeit less pronounced aspect determining $\beta_{\rm eff}$ is the β-dependence of $E_{\rm post}(\beta)$ for the interacting post-quench system. Here we find that with increasing inter-orbital coupling V, the same amount of total energy leads to a lower effective temperature. Note that for the spinless Chern insulator, the Hubbard repulsion U is missing. Therefore, ΔE is smaller than for the spinfull model, leading to a lower effective temperature and larger steady-state Hall response.

B. Slow ramps

The injected energy ΔE can be controlled by ramping the gap parameter instead of a sudden quench. This leads to the steady-state (spin) Hall response approaching the quantized value in Fig. 4 in the main text. Figure 6 shows the corresponding dependence of $T_{\rm eff} = 1/\beta_{\rm eff}$. In the limit of infinitely slow ramps ($t_{\rm ramp} \to \infty$), the injected energy ΔE tends to zero, as all transitions induced by the ramp become adiabatic. The only exception is the Γ point (where the gap closing occurs) – transitions there are never adiabatic since the gap passes through zero. Therefore, the occupation in the upper band $f_+(\mathbf{k})$ is exponentially small, except for $f_+(\mathbf{k} \approx \Gamma)$. The number of carriers in the upper band $N_+ = 1/N_k \sum_{\mathbf{k}} f_+(\mathbf{k})$, however, becomes arbitrarily small with increasing $t_{\rm ramp}$. Hence, the system thermalizes at an arbitrarily low $T_{\rm eff}$. The exponential decrease of $T_{\rm eff}$ as a function of $t_{\rm ramp}$ is demonstrated in Fig. 6.

V. SCALING OF PURITY GAP CLOSING

In the main text, we have discussed the purity gap closing characterized by the critical time $t_{\rm crit}$. In order to investigate the dependence on the interaction, we have computed $t_{\rm crit}$ for additional values of the interaction strength for both the Chern insulator with local interactions only and including nonlocal interactions. The result is presented in Fig. 7.

Linear regression of $\log(t_{\rm crit})$ as a function of $\log(V)$ shows that in the scenario with or without nonlocal interactions the critical time approximately scales as $\sim V^{-3/2}$. Interstingly, the long-time relaxation times scale as $\sim V^{-2}$; hence, the time scale of the purity gap closing is different from thermalization and more related to dephasing effects.

Furthermore, we have analyzed the dependence of $t_{\rm crit}$ on $M_{\rm pre}$ and $M_{\rm post}$. The result is shown in the bottom panels of Fig. 4. Again, we find that there is almost no dependence on $M_{\rm pre}$, while increasing $M_{\rm post}$ leads to significantly faster $t_{\rm crit}$. In comparison to the upper panels in Fig. 4, one finds that injecting more energy into the system accelerates the purity gap closing. This is expected, as particle-particle scattering is enhanced if more excited carriers are present in the conduction band. Therefore, the dephasing time scale and thus $t_{\rm crit}$ become faster. In terms of a fast topological phase transition, injecting a larger amount of energy is favourable; however, the steady-state Hall response becomes smaller.

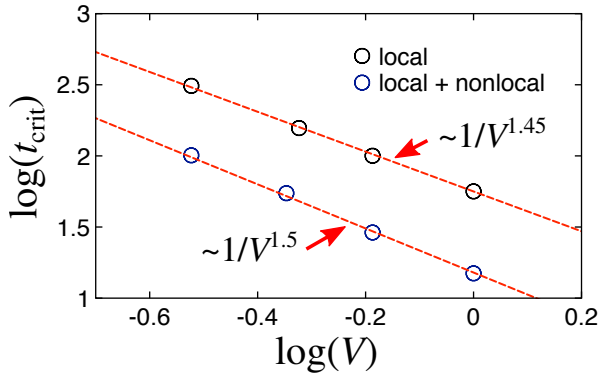

FIG. 7. Double-logarithmic plot of the critical time of the purity gap closing as a function of the interaction strength.

[1] G. Stefanucci and R. v. Leeuwen, *Nonequilibrium Many-Body Theory of Quantum Systems: A Modern Introduction* (Cambridge University Press, 2013).
[2] M. Schüler, Y. Murakami, and P. Werner, Phys. Rev. B **97**, 155136 (2018).
[3] P. Lipavsky, V. Spicka, and B. Velicky, Phys. Rev. B **34**, 6933 (1986).
[4] A. Alvermann and H. Fehske, J. Comput. Phys. **230**, 5930 (2011).
[5] N. Schlünzen and M. Bonitz, Contributions to Plasma Physics **56**, 5 (2016).
[6] S. Latini, E. Perfetto, A.-M. Uimonen, R. van Leeuwen, and G. Stefanucci, Phys. Rev. B **89**, 075306 (2014).